

Nanoengineered Au-carbon nitride interfaces enhance photocatalytic pure water splitting to hydrogen

Ingrid F. Silva^{#,a,b}, Soumyabrata Roy^{#,*,c}, Pawan Kumar^{#,d}, Zhiwen Chen^e, Ivo F. Teixeira^f,
Astrid Campos-Mata^c, Loudiana M. Antônio^g, Luiz O. Ladeira^g, Humberto O. Stumpf^h,
Chndra Veer Singh^e, Ana Paula C. Teixeira^a, Md Golam Kibria^{*,d}, Pulickel M. Ajayan^{*,c}.

^aDepartamento de Química, ICEx, Universidade Federal de Minas Gerais, Belo Horizonte, MG, 31270-901, Brazil.

^bDepartment of Colloid Chemistry, Max Planck Institute of Colloids and Interfaces, Am Mühlenberg 1, D-14476 Potsdam, Germany.

^cDepartment of Materials Science and NanoEngineering, Rice University, Houston, Texas 77005, USA.

^dDepartment of Chemical and Petroleum Engineering, University of Calgary, 2500 University Drive, NW Calgary, Alberta, Canada.

^eDepartment of Material Science and Engineering, University of Toronto, Ontario, Canada.

^fDepartamento de Química, Universidade Federal de São Carlos, São Carlos, SP, 13565-905, Brazil.

^gDepartamento de Física, ICEx, Universidade Federal de Minas Gerais, Belo Horizonte, MG, 31270-901, Brazil.

^hEqual contribution

Contents

1. Experimental section

1.1. Syntheses of CN(M) and CN(T).....	Page S2
1.2. Synthesis of Au NPs solution with an average diameter of 7 nm.....	Page S2
1.3. Synthesis of Au NPs solution with an average diameter of 14 nm.....	Page S2
1.4. Synthesis of Au NRs solution with an average diameter of 65 nm.....	Page S3
1.5. Synthesis of Au NRs solution with an average diameter of 15 nm.....	Page S3
1.6. Preparation of Au CN(T) composites using the incipient wetness method.....	Page S4
1.7. Characterizations.....	Page S4
1.8. Hydrogen evolution experiments.....	Page S7
1.9. Computational Methods.....	Page S8

2. Results and Discussion

2.1. TEM.....	Page S9
2.2. Synchrotron-based Wide-angle X-ray scattering (WAXS) and XRD.....	Page S10
2.3. TG and DTG analysis.....	Page S14
2.4. XPS.....	Page S15
2.5. C K-edge and N K-edge NEXAFS spectra of the materials.....	Page S16
2.6. Steady-state photoluminescence (PL).....	Page S17

3. References

Figures

Figure S1. TEM images for the CNs.....	Page S9
--	---------

<i>Figure S2. TEM images for the Au-CNs nanocomposites</i>	<i>Page S10</i>
<i>Figure S3. Synchrotron-based WAXS of CN(M), CN(T) and CN(T)-7-NP</i>	<i>Page S12</i>
<i>Figure S4. Fitting of the Gaussian profiles of Au-CNs nanostructures peaks in the powder X-ray diffractogram</i>	<i>Page S13</i>
<i>Figure S5. TG and DTG curves of Au-CNs</i>	<i>Page S14</i>
<i>Figure S6. XPS spectra of CN(T)-14-NP, CN(T)-65-NR and CN(T)-15-NR</i>	<i>Page S15</i>
<i>Figure S7. Excitation-Emission Matrix Spectroscopy (EEMS) map of materials</i> ...	<i>Page S17</i>
<i>Figure S8. PL and TRPL spectra</i>	<i>Page S18</i>
<i>Figure S9. Local density of states of Au₁₃@CN without and with defects</i>	<i>Page S20</i>
<i>Figure S10. Geometric adsorption structures of H₂O* and HO*-H*</i>	<i>Page S21</i>

Tables

<i>Table S1. The TRPL components and their contribution</i>	<i>Page S18</i>
<i>Table S2. EIS fitting parameters and determined components</i>	<i>Page S19</i>
<i>Table S3. Comparison of pure water photo-splitting catalysts</i>	<i>Page S19</i>

1. Experimental section

1.1. Synthesis of CN(M) and CN(T)

CN(M) and CN(T) were prepared by the modified method reported by Silva et al.¹ 3.0 g (23.8 mmol) of melamine and 3.0 g (39.4 mmol) of thiourea were placed in a porcelain crucible for CN(M) and CN(T) syntheses, respectively. The crucible was covered, placed in a muffle furnace and heated to 550 °C for 30 min, using a heating rate of 10 °C min⁻¹. After the crucible was completely cooled, the obtained yellow solid was ground and used for further modifications. (Yield: CN(M) 43% and CN(T) 9%).

1.2. Synthesis Au NPs solution with an average diameter of 7 nm (Au-7-NP)

Gold nanospheres with an average diameter of 7 nm were synthesized using the method described by Simpson *et al.*² 240 µL of chloroauric acid (HAuCl₄) (0.1 M); 0.251 g of glutathione (C₁₀H₁₇N₃O₆S) and 0.0153 g of sodium hydroxide (NaOH) were added to 50.0 mL of deionized water with stirring. Then, 476 µL of sodium borohydride (NaBH₄) (0.25 M) was added to the solution. The reaction ends when the solution turns a dark red color.

1.3. Synthesis Au NPs solution with an average diameter of 14 nm (Au-14-NP)

The synthesis of gold nanospheres with an average diameter of 14 nm was performed using the standard citrate reduction method described by Turkevich and collaborators.³ In brief, 50

mL of a HAuCl₄ solution (29.4 mM) was heated to 80 °C. Then, 5 mL aqueous solution of trisodium citrate (C₆H₅Na₃O₇) (1% w/v) was added to the obtained solution. The reaction reaches completion when the solution turns red (after approximately 20 min).

1.4. Synthesis Au NRs solution with an average diameter of 65 nm (Au-65-NR)

The synthesis of gold nanorods was performed using the seed-mediated method, described by Nikoobakht and El-Sayed.⁴ The method consists of adding a seed solution, containing gold nanospheres of 3 nm in diameter, in a solution of growth containing Au⁺ ions. The seed solution was prepared by adding 5 mL of HAuCl₄ (0.0005 M) to 5 mL of the CTAB surfactant (0.2 M) followed by the addition of 600 µL of the strong NaBH₄ reducer (0.01 M). After the addition of NaBH₄, there was the formation of a brownish solution containing 3 nm nanospheres. This seed solution remained in a water bath for 1 h at 30 °C. The growth solution was prepared by adding 5 mL of HAuCl₄ (0.001 M) to 5 mL of the CTAB surfactant (0.2 M) followed by the addition of 200 µL silver nitrate (AgNO₃) (0.004 M) and 70 µL of the weak ascorbic acid (C₆H₈O₆) reducer (0.0788 M). After the addition of ascorbic acid, the solution becomes transparent, as Au³⁺ is reduced to Au⁺. Then, 12 µL of the seed solution was added to the growth solution (longitudinal peak at 650 nm). After a few minutes, the formation of gold nanorods begins and this new mixture was kept in a water bath for 24 h at 30 °C. The size of the nanorods is determined by the amount of seed solution added to the growth solution.

1.5. Synthesis Au NRs solution with an average diameter of 15 nm (Au-15-NR)

The synthesis of gold nanorods was performed using the seed-mediated method, described by Nikoobakht and El-Sayed.⁴ The seed solution was prepared by adding 5 mL of HAuCl₄ (0.0005 M) to 5 mL of the CTAB surfactant CTAB (0.2 M) followed by the addition of 600 µL of the strong NaBH₄ reducer (0.01 M). After the addition of NaBH₄, there was the formation of a brownish solution containing 3 nm nanospheres. This seed solution remained in a water bath for 1 h at 30 °C. The growth solution was prepared by adding 5 mL of HAuCl₄ (0.001 M) to 5 mL of the CTAB (0.2 M) followed by the addition of 200 µL AgNO₃ (0.004 M) and 70 µL of the weak ascorbic acid (0.0788 M). After the addition of ascorbic acid, the solution becomes transparent, as Au³⁺ is reduced to Au⁺. Then, 500 µL of the seed solution was added to the growth solution (longitudinal peak at 770 nm). After a few minutes, the

formation of gold nanorods begins and this new mixture was kept in a water bath for 24 h at 30 °C.

1.6. Preparation of Au CN(T) composites using the incipient wetness method

7 mL of each Au metal solution with an average diameter of: Au NPs of 7 nm, Au NPs of 14 nm, Au NRs of 65 nm and Au NRs of 15 nm, respectively, were added dropwise to 200 mg of CN(T) material with a controlled temperature of 90 °C. The drops were added to the solid, and mixed so that the Au metal impregnation was homogeneous and dried. Several cycles like this were done until the 7 mL of Au metal was finished. The obtained solid was dried under a vacuum for 24 h. The Au composites were named: CN(T)-7-NP, CN(T)-14-NP, CN(T)-65-NR, CN(T)-15-NR, respectively.

1.7. Characterizations

The elemental composition analyses of carbon, hydrogen, nitrogen and sulfur were accomplished using a Vario Micro device. Inductively coupled plasma-optical emission spectrometry (ICP-OES) was performed using a Horiba Ultra 2 instrument equipped with photomultiplier tube detector. The samples for ICP-OES were prepared by dissolving materials in concentrated HCl:HNO₃ solution followed by dilution and filtration. The spectra in the infrared region were acquired by ATR (Attenuated Total Reflectance) on a Varian 1000 FT-IR spectrometer equipped with an attenuated total reflection unit with diamond crystal. The spectra were obtained in the region of 650 to 4000 cm⁻¹ with a spectral resolution of 0.5 cm⁻¹. The measurements of mass variation as a function of temperature, Thermogravimetric Analysis (TGA), were performed using a Shimadzu TGA-60H thermobalance. The apparatus was operated in the temperature range of approximately 25 to 900 °C. Analyses were performed accomplished using a flow rate of 50 mL min⁻¹ of synthetic air at a heating rate of 10 °C min⁻¹ in an alumina crucible. The X-ray powder diffraction (p-XRD) measurements were recorded on a Bruker D8 Advance diffractometer equipped with a scintillation counter detector with CuK α radiation ($\lambda = 0.15418$ nm) applying a 2θ step size of 0.05° and counting time of 3s per step. Steady-state UV-vis absorption spectra were obtained using Shimadzu UV 2600 in diffuse reflectance mode. The Transmission Electron Microscope (TEM) images were performed using the Tecnai G2-20 (FEI) equipment with a voltage of 200 keV. The powder samples were dispersed in isopropanol, immersed in an ultrasonic bath for 10

minutes, and deposited in copper grids the type Holey Carbon with 200-mesh of EMS. The Mott-Schottky measurements were recorded in an Electrochemical BAS Epsilon system using 3 electrodes set up consisting of a Pt wire working as counter electrode, an Ag/AgCl (3M KCl) as reference electrode, F-doped tin oxide (FTO) glass coated with the material as a working electrode. The working electrode was prepared on FTO glass that was cleaned by sonication in ethanol for 30 min and dried at 353 K. The contact boundary of FTO glass was protected using Scotch tape. 3 mg of each sample was dispersed in 1 mL of water and 20 μ L of Nafion by sonication to get a slurry mixture. The slurry was spread onto pretreated FTO glass. After air-drying, the Scotch tape was removed and the working electrode was further dried at 393 K for 2 h to improve adhesion. After this time, the measurements were carried out in a Na₂SO₄ solution (0.5 M). The scattered photoluminescence (PL) spectra were obtained in the fluorescence spectrometer Jasco FP-8300 with excitation wavelength was set to 370 nm in all analyses and under air. X-ray photoelectron spectroscopy (XPS) measurements were performed on a ThermoScientific Escalab 250 Xi. A microfocused, monochromated Al K α X-ray source (1486.68 eV) and a 400 μ m spot size were used in the analysis. Samples were prepared using carbon tape. LiCl was added to each sample to calibrate the binding energies towards Li. ThermoScientific Avantage software was used to analyze the resulting spectra. The electrochemical properties of materials were investigated using an Autolab electrochemical workstation using a three-electrode setup. The working electrode was an FTO glass coated with a 10 nm TiO₂ blocking layer.⁵ The catalyst was dispersed in DMF and α -terpineol followed by sonication to make a homogeneous solution. A certain amount of the obtained suspension was drop-cast on FTO followed by evaporation of solvent at 170 °C. Finally, the materials deposited on the anode were covered with a parafilm window for the measurement. Pt was used as a counter electrode (cathode) while Ag/AgCl electrode was used as the reference electrode. All the measurements were performed in 0.5 M Na₂SO₄. Electrochemical impedance spectroscopy (EIS) for Nyquist plots to determine the semiconductor-electrolyte interaction was performed under dark and AM1.5 G solar irradiation (Power density: 100 mA cm⁻²; HAL-320 Solar Simulator, Class A, 300 W Xe lamp). The EIS measurement was performed in a three-electrode setup at an applied bias of -0.5 V vs Ag/AgCl, with an AC amplitude of 5 mV at a frequency of 100 kHz. To evaluate the charge generation capability of the materials photoelectrochemical

measurements were also performed. The photocurrent response of materials under dark and light illumination was determined by measuring photocurrent density (J) as a function of time (J - t curve) during light on-off cycles at water oxidation potential (+0.6 V vs Ag/AgCl).

To elucidate the local chemical structure and coordination pattern of the materials, synchrotron-based X-ray absorption spectroscopy using soft X-rays (sXAS) was performed. The XAS analysis was performed at the Canadian Light Source (CLS) synchrotron's spherical grating monochromator (SGM) beamline (CLS port 11ID-1) operating in the energy range of 250 to 2000 eV. The chamber was kept at an ultrahigh vacuum ($\sim 10^{-6}$ Torr) and measurements were performed at room temperature. The samples were deposited on a sample holder using double-sided carbon tape and mounted in a vacuum chamber at 45° w.r.t. to beam and detector. After evacuation the samples were irradiated with soft X-ray and spot size was kept at 50- and 100- μm using the Kirkpatrick-Baez mirror system. The counts and energy of photons emitted in the process of core hole filling were measured using Amptek silicon drift detectors (SDDs) with an energy resolution of ~ 100 eV. The Partial fluorescence yield was reported and the SDD detector's signal was reported due to the appropriate location. Additionally, total electron yield (TEY) was also measured. After mounting the sample in the vacuum chamber Excitation-Emission Matrix Spectroscopy (EEMS) measurements in the energy range of 250 to 2000 eV (energy resolution ~ 5 eV) were performed to get the information of each element present in the sample. An EEMS map was accumulated by averaging 10 scans with an exposure time of 1 min. The samples were moved 0.1 mm to eliminate the possibility of radiation damage to the sample. The C K-edge and N K-edge were scanned, and final spectra were accumulated by averaging the PFY of ten consecutive measurements. Since Au edges were beyond the energy range of the beamline they were not measured. The live data processing channel (SGM beamline laboratory acquisitions and analysis system) was used for the data processing and averaging of the EEMS and NEXFAS signals.

To investigate the nanocrystalline attributes and lattice spacing of the materials synchrotron-based wide-angle X-ray scattering (WAXS) measurements were carried out at 04ID-1 BXDS-WLE Low Energy Wiggler Beamline of a Canadian light source. The beamline energy range for BXDS-WLE is 7-22 keV, with a maximum photon flux of 1×10^{12} to $5 \times$

1012 photons s^{-1} in focus on the sample at 250 mA ring current. The typical spot size was 150 μm vertical x 500 μm . Other parameters were as follow: resolution: $\Delta E/E$, Si (111): 2.8×10^{-4} at 7.1 keV to 6.4×10^{-4} at 15.9 keV. Si (311): 2.5×10^{-4} at 12.9 keV to 4.5×10^{-4} at 22.5 keV, photon energy: 15116 eV ($\lambda = 0.8202 \text{ \AA}$) using Si(111) and default detector: Dectris Mythen2 X series 1K. The measurements were performed on powder samples by depositing a small powder on glass slides followed by mounting it on a multisample holder. The X-ray wavelength was 0.8202 nm (15116 keV) while the detector distance was 170 mm. A LaB6 sample was used as a calibration standard to measure the q-1 value and obtained results were compared with the reported value. The q-1 values d-spacing and other parameters of the LaB6 sample are also available on the CLS site: <https://brockhouse.lightsource.ca/about/low-energy-wiggler-beamline/>.⁶ The acquired .xye files were processed in GSAS-II software to calculate q-1 and d-spacing.

1.8. Hydrogen evolution experiments

The photocatalytic performance of pure CNs and Au-CN(T) nanostructures were investigated for the water splitting with/without any sacrificial donor under solar simulated light conditions. Initially, the photocatalytic performance was evaluated by using triethanolamine (TEOA) as a sacrificial donor to screen the optimum performing catalyst. After that, all the catalysts were evaluated for pure water photo-splitting and a time-dependent H_2 evolution profile was also measured. In brief, a 30 mL borosil® glass vial was charged with 10 mg of catalysts and HPLC grade water (10 mL)/TEOA (100 μL) and the obtained suspension was sonicated for 15 min. The vial was sealed with Aluminum Crimp Cap with PTFE septum. The mixture was purged with nitrogen under stirring for 30 min to remove any dissolved oxygen and headspace O_2 . Then an empty balloon was connected to the vial for collecting the photoreaction gaseous mixture. The reaction mixture was irradiated under AM1.5 G irradiation using a solar simulator with a power density of 100 mW cm^{-2} at the surface of the vial. After a certain interval, the reaction mixture was withdrawn from the vial using a gas-tight syringe and injected into the GC equipped with a Molsieve column and TCD/FID detector. For the product quantification standard gaseous mixture containing H_2 was also injected in GC. A calibration curve was made by injecting different amounts of the mixture to ensure a linear response of GC. The resiliency of the catalyst for the long runs was

evaluated by evacuating and purging the vial followed by irradiation and measuring the evolved hydrogen. The wavelength-dependent H₂ evolution was measured using four monochromatic irradiations (450, 520, 590, 620 nm) while keeping a power density of 25 mW cm⁻². Further, we have calculated the performance of samples after annealing at 350 °C.

1.9. Computational Methods

Spin-polarized density functional theory (DFT) was carried out through using the Vienna *ab initio* simulation package (VASP).⁷ The interactions between valence electrons and ionic cores were described by the projector-augmented wave (PAW) pseudopotential and the exchange-correlation effects were considered by the Perdew-Burke-Ernzerhof (PBE) exchange-correlational functional with generalized gradient approximation (GGA).^{8,9} The wave function calculation applied the kinetic energy cutoff energy of 550 eV. The vacuum gap was more than 12 Å to neglect interactions between the system and its mirror images. DFT-D3 method was used to correct the van der Waals interaction.¹⁰ During the geometrical optimization, the convergence criteria were set to be 1×10^{-5} eV for energy change and 0.02 eV Å⁻¹ for force change. The Monkhorst-Pack *k*-points were $2 \times 2 \times 1$ for all systems with the lattice parameter of $a = b = 14.242$ Å. Bader charges were considered to analyze the properties of charge transfer.¹¹ The transition states were investigated using the climbing image nudged elastic band method with an energy accuracy of 1×10^{-5} eV and interatomic forces of less than 0.05 eV Å⁻¹.

2. Results and Discussion

2.1. TEM

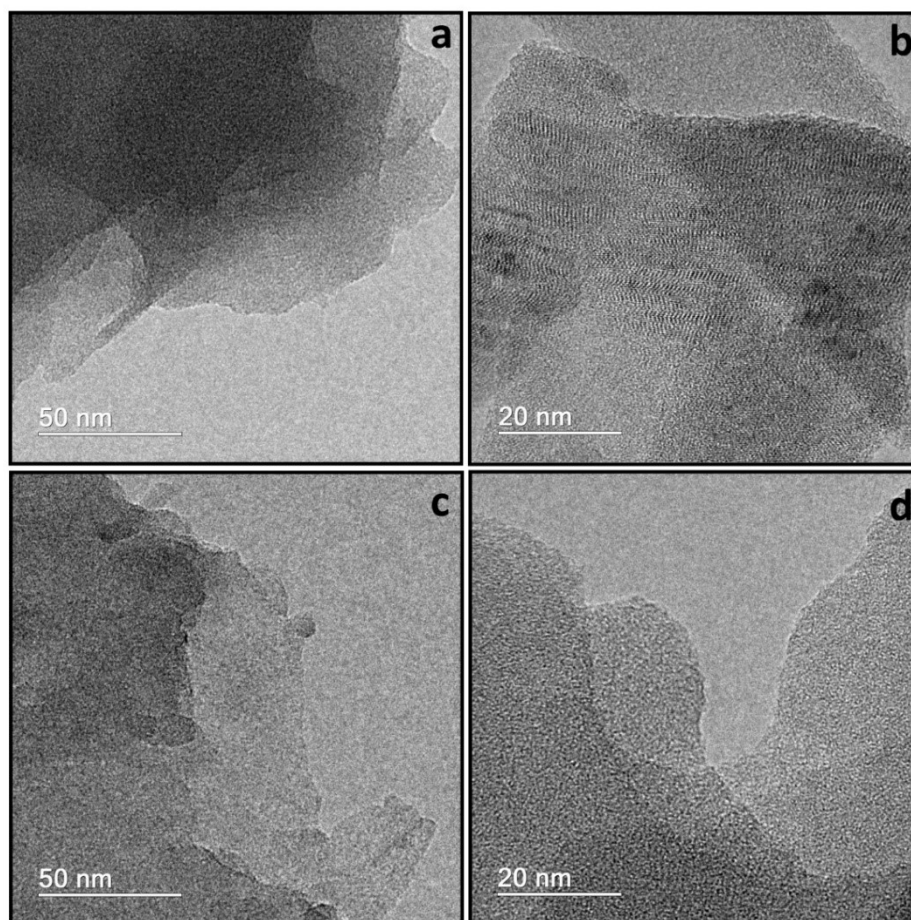


Figure S1. TEM images for the CNs. a) and b) CN(M); c) and d) CN(T).

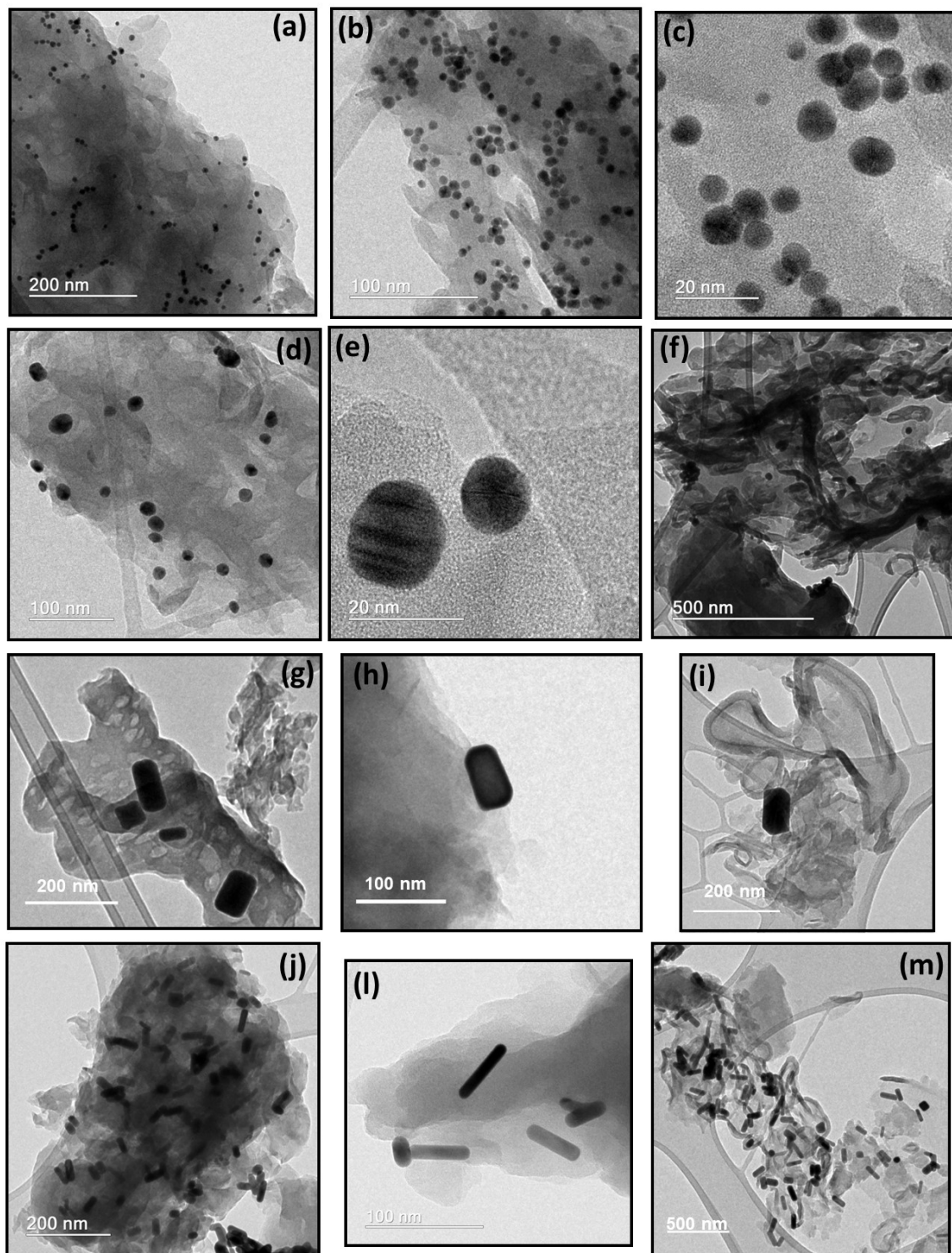


Figure S2. TEM images for the Au-CNs nanocomposites. (a), (b) and (c) CN(T)-7-NP; (d), (e) and (f) CN(T)-14-NP; (g), (h) and (i) CN(T)-65-NR; (j), (l) and (m) CN(T)-15-NR.

2.2. 2D WAXS and XRD

Synchrotron-based Wide-angle X-ray scattering (WAXS)

Synchrotron-based Wide-angle X-ray scattering (WAXS) was employed to investigate the nanocrystalline and stacking features of the materials. The coherent, narrow wavelength, monochromatic synchrotron-based X-ray radiation allows better spectral resolution and peak intensities thus giving insight into the material structural attributes.¹²⁻¹⁵ The wavelength of BXDS-WLE beamline X-ray radiation was 0.8202 Å which was almost half of the magnitude of CuK α radiation (1.5418 Å) thus a better resolution was accomplished. Since 2θ values are dependent on the incident wavelength thus it is not a valid measure to make a fair comparison. On the other hand, the Q value (\AA^{-1}) which is independent of incident X-ray wavelength is an ideal parameter to compare the lattice parameters. So, the Q values (in \AA^{-1}) along with the obtained d-spacings are provided to compare the results with existing data. The WAXS 2D map image of the CN displayed two intense diffraction rings due to 100 and 002 plane reflections (**Figure S5a**).¹⁶ The intense 002 plane peak arise due to interplanar stacking of C₆N₇ constituted conjugated sheets while the (100) peak originated from the periodic in-plane arrangement of C₆N₇ units. The calculated Q⁻¹ value for 100 and 002 peaks was found to be 0.92 and 1.93 \AA^{-1} corresponding to 6.94 and 3.33 Å d-spacing (**Figure S5d**). In addition to these main peaks, very faint bands around 3.01 and 3.77 \AA^{-1} were assigned to 300 and 004 planes of melon. Interestingly, these peaks remain obscured in the regular XRD and evidently represent the superiority of synchrotron-based radiation.

It should be noted that all these features of carbon nitride were also present in defect-rich CN(T) samples demonstrating the basic carbon nitride scaffold remain intact even after structural defects (**Figure S5b and e**) The WAXS 2D map and spectra of CN(T)-7-NP exhibited many intense rings/peaks associated with Au gold nanoparticles (**Figure S5c and f**). Compared to pristine CN and defect-rich CN(T) the peaks corresponding to the carbon nitride framework were relatively weak suggesting that the incorporation of Au followed by ligand removal introduce slight structural deformation.

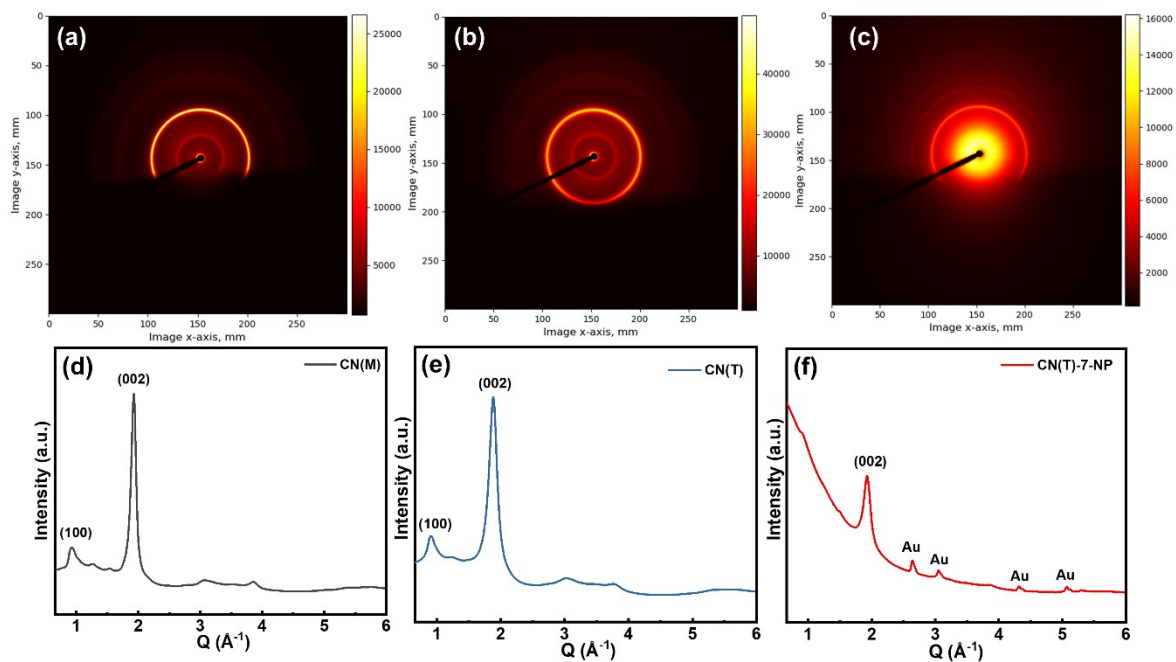


Figure S3. Synchrotron-based WAXS 2D images and obtained Q^{-1} values of **(a)** and **(d)** CN(M); **(b)** and **(e)** CN(T); **(c)** and **(f)** CN(T)-7-NP, respectively.

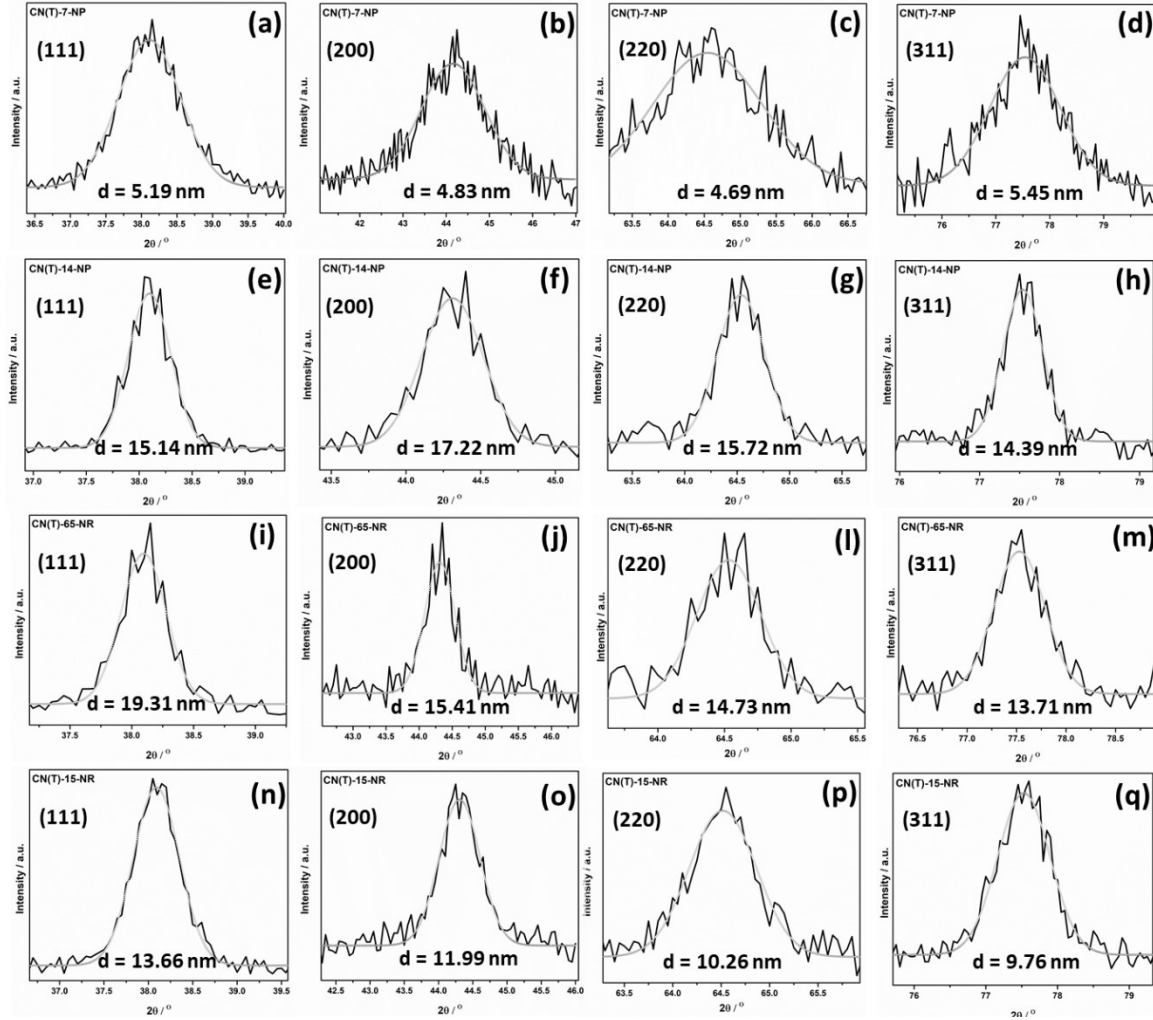


Figure S4. Fit with Gaussian profiles of Au-CNs nanostructures peaks in the powder X-ray diffractogram at 38.1° , 44.3° , 64.5° and 77.6° , which is attributed to (111), (200), (220) and (311) planes, respectively, of metallic gold (Au^0) with cubic structure (JCPDS Card No. 04-0784) of (a), (b), (c) and (d): CN(T)-7-NP; (e), (f), (g) and (h): CN(T)-14-NP; (i), (j), (l) and (m): CN(T)-65-NR; (n), (o), (p) and (q): CN(T)-15-NR.

Scherrer equation

By the use of the Scherrer equation (**Eq. S1**) it is possible to describe quantitatively the average size of the crystallites (T).^{17,18} This equation is valid when the crystals are smaller than $0.1\ \mu\text{m}$.¹⁹

$$\text{(Eq. S1)}$$

where k is the proportionality constant, which ranges from 0.68 to 2.08. The value used in this equation for the analyzed materials was $k = 0.9$. λ (Å) is the wavelength of the X-

rays. For this experiment, a copper tube with an average $K\alpha = 1.54178 \text{ \AA}$ was used. $Beta$ (β) is the FWHM, it is obtained by the difference between two extreme values of an independent variable in which it, the function, reaches half of its maximum value. $Theta$ (θ) is the Bragg angle; it is half the peak position on the diffractogram.

2.3. TG and DTG curves

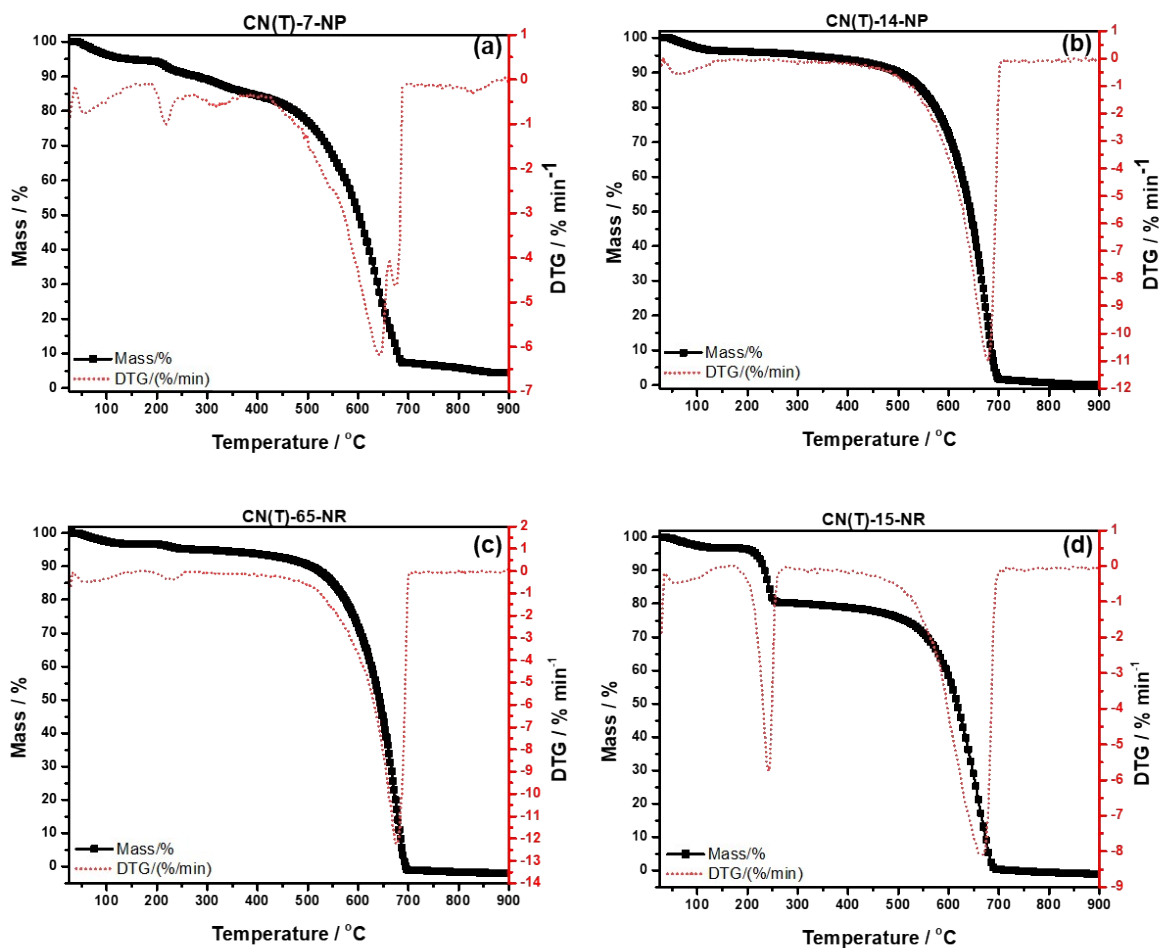


Figure S5. TG and DTG curves of Au-CN_s synthesized materials performed in a dynamic atmosphere of air synthetic (50 mL min^{-1}) in an alumina crucible with a heating rate of $10 \text{ }^\circ\text{C min}^{-1}$.

2.4. XPS

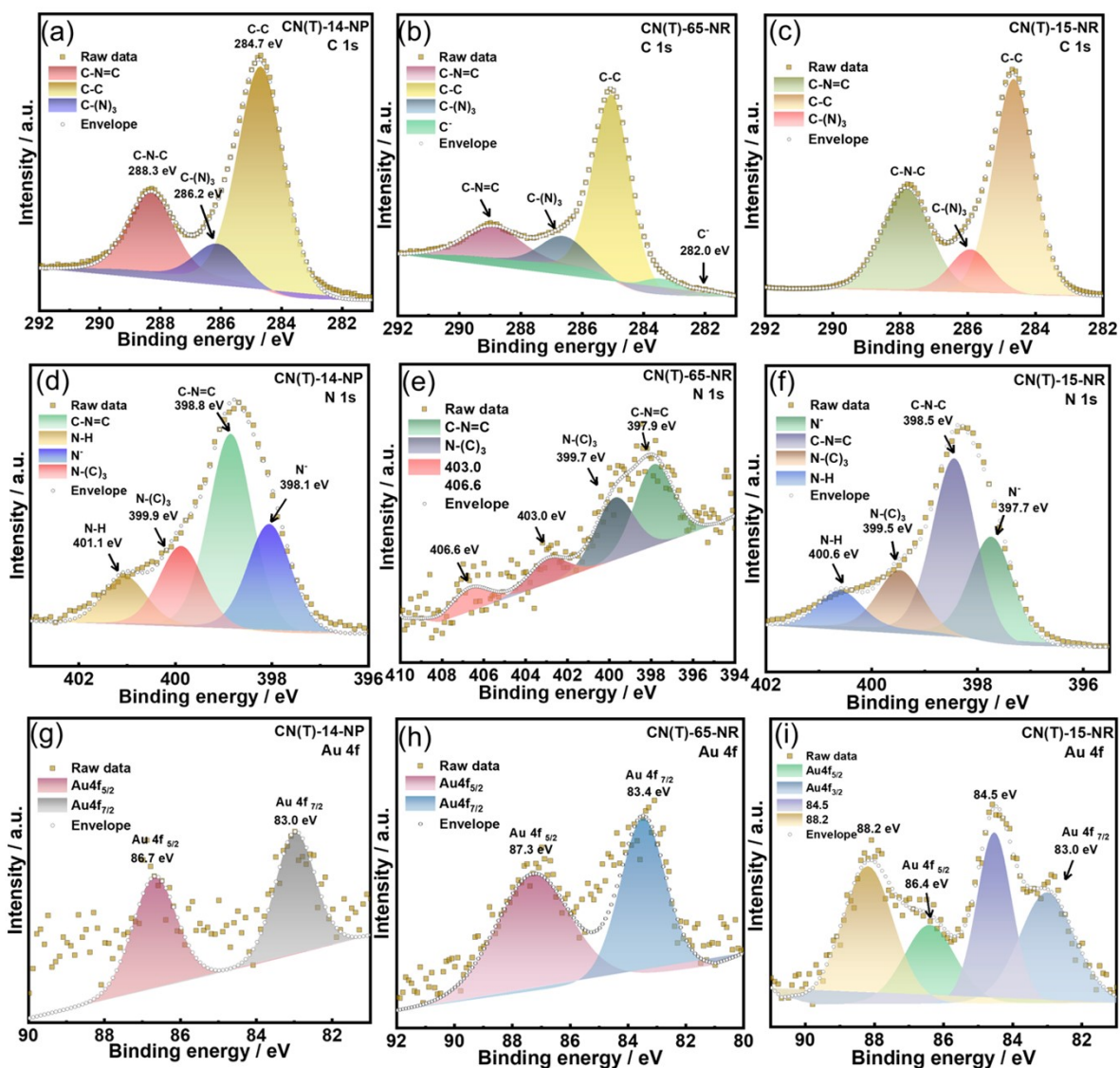


Figure S6. C 1s, N 1s and Au 4f high-resolution XPS spectra of CN(T)-14-NP, CN(T)-65-NR and CN(T)-15-NR materials. (a), (b) and (c) C 1s high-resolution XPS spectra of CN(T)-14-NP, CN(T)-65-NR and CN(T)-15-NR materials, respectively. (d), (e) and (f) N 1s high-resolution XPS spectra of CN(T)-14-NP, CN(T)-65-NR and CN(T)-15-NR materials, respectively. (g), (h) and (i) Au 4f high-resolution XPS spectra of CN(T)-14-NP, CN(T)-65-NR and CN(T)-15-NR materials, respectively.

2.5. C K-edge and N K-edge Near Edge X-Ray Absorption Fine Structure (NEXAFS) spectra of the materials

To deduce the local electronic environment and coordination state of the materials synchrotron-based near-edge X-ray absorption fine structure (NEXAFS) spectroscopy was performed using soft X-ray at the SGM beamline of Canadian Light Source, Canada. The C-K-edge excitation-emission matrix spectroscopy (EEMS) map of all the samples displayed a sharp emission band around ~ 285 eV demonstrating an abundance of carbon in all materials (**Figure S4a**). **Figure S4b** displays panel carbon K-edge NEXAFS spectra of all the materials. The C K-edge NEXAFS spectra of pristine carbon nitride (CN), defect-rich carbon nitride CN(T) and Au CN(T) nanohybrids exhibited two signature π^* resonance peaks located at 284.6 and 287.5 eV.²⁰ The weak resonance peak at 284.6 eV originated due to the $\pi^*_{\text{C=C}}$ transition in uncondensed functionalities and carbon adventitious carbons. Another sharp peak at 287.5 eV was attributed to the $\pi^*_{\text{N-C=N}}$ transition in N-linked heptazine (C_6N_7) moieties.²¹ Interestingly, the pristine CN sample does not have any detectable $\pi^*_{\text{C=C}}$ resonance peak while the CN(T) and Au CN(T) displayed a rise of $\pi^*_{\text{C=C}}$ signals. The increased $\pi^*_{\text{C=C}}$ intensity suggests that defects incorporation in CN structure introduces N deficient sites thus intensifying C=C transitions. Further, the use of organic C-rich ligands during the synthesis step might also contribute to the $\pi^*_{\text{C=C}}$ resonance. Furthermore, the high-energy region of C K-edge NEXAFS unveils a broader σ^* region originated from $\text{sp}^2 \sigma^*_{\text{N-C=N}}$ and $\text{sp}^3 \sigma^*_{\text{C-N}}$ transitions. The EEMS map of all samples displayed an intense band around ~ 400 eV attributed to the N K-edge validating N rich character of the materials (**Figure S4c**). The N K-edge NEXAFS spectra of CN, CN(T) and all other Au-containing samples exhibited two π^* resonance peak at 399.3 and 402.2 eV corresponding to $\pi^*_{\text{C-N=C}}$ transition of nitrogen in heptazine (C_6N_7) unit and $\pi^*_{\text{N-C}_3}$ of bridging nitrogen (**Figure S4d**).^{22,23} Additionally, a broad peak band in the σ^* region originated due to $\text{sp}^2 \sigma^*_{\text{C-N=C}}$ and $\text{sp}^3 \sigma^*_{\text{C-N}}$ transitions. The obtained results suggest that despite the presence of plenty of defective states the basic N-linked heptazine framework remains intact.

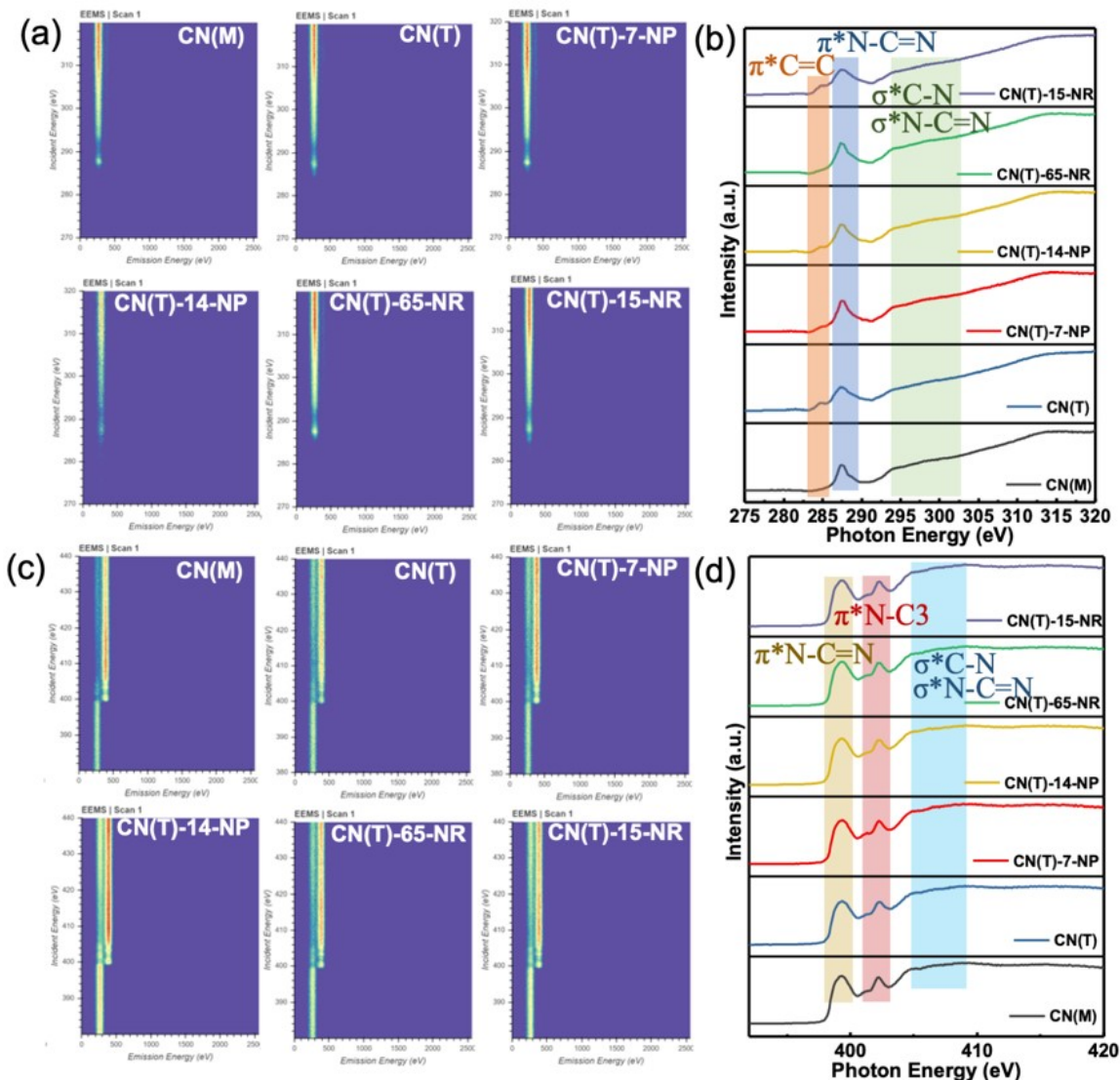


Figure S7. Excitation-Emission Matrix Spectroscopy (EEMS) map of CN(M), CN(T), CN(T)-7-NP, CN(T)-14-NP, CN(T)-65-NR and CN(T)-15-NR showing (a) C K signal (c) N K signals and corresponding NEXAFS spectra in (b) C K-edge showing π^* and σ^* transition (d) C K-edge showing π^* and σ^* resonance peaks.

2.6. Steady-state photoluminescence (PL)

The steady-state PL spectra were obtained under an excitation wavelength of 370 nm and showed a peak centered around 450 nm for the synthesized materials (**Figure S6a**). PL spectra of CN(T) displayed a relatively intense peak compared to CN(M) attributed to enhanced radiative recombination in defect-rich carbon nitride. Previous reports also demonstrate the presence of NH_2 defects states promote severe localized recombination.²⁴ Interestingly, after the integration of Au nanostructures, the PL intensity profile of all Au-CN(T) samples was increased which was assumed due to the injection of electrons from Au to CN structure followed by the radiative recombination process. Contradicting TRPL

findings, the increased PL intensity suggests in addition to working as an electron sink, Au nanostructures can also pump electrons to the CN scaffold. Considering the fact that NH_2 provides intermediate sub-energy, thus more $\text{C-N}\pi \rightarrow \text{NH}_2 \sigma^*$ electronic transition is taking place in defect-rich carbon nitride. In addition, previous studies suggest that NH_2 conjugated with aromatic graphene structure can extend conjugation degree and also delay recombination, leading to better performance.²⁵ Furthermore, Au nanoparticles increased the surface properties of the matrix and improved charge separation by plasmon exciton coupling.

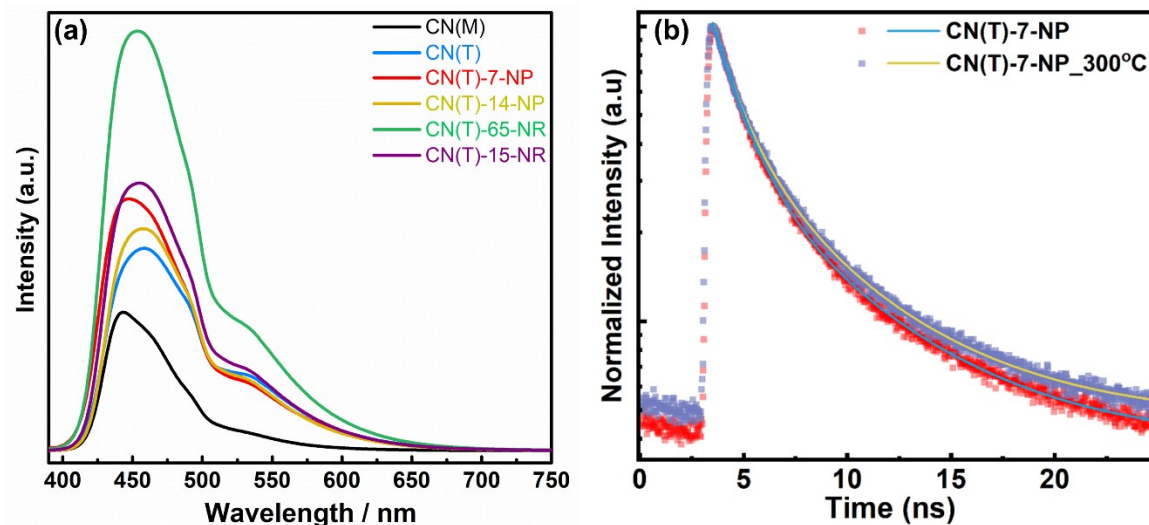


Figure S8. (a) Steady-state photoluminescence emission spectra and (b) Time resolved photoluminescence (TRPL) spectra of CN(T)-7-NP and CN(T)-7-NP_300 °C.

Table S1. The PL lifetime decay components and their contribution. The average lifetime (τ_{avg}) of each sample

Sample	τ_1 (ns)	A_1	τ_2 (ns)	A_2	τ_3 (ns)	A_3	R^2	τ_{avg} (ns)
CN(M)	1.21 ± 0.22	0.34	2.75 ± 2.05	0.29	6.9 ± 2.62	0.30	0.9991	5.18
CN(T)	1.26 ± 0.55	0.21	2.77 ± 4.14	0.18	7.96 ± 7.11	0.35	0.9952	6.75
CNT(T)-7-NP	1.06 ± 0.25	0.41	1.88 ± 1.31	0.27	5.53 ± 0.80	0.27	0.9992	3.98
CNT(T)-14-NP	1.06 ± 0.22	0.40	1.91 ± 1.16	0.28	5.47 ± 0.73	0.28	0.9993	3.95
CNT(T)-65-NR	1.14 ± 0.72	0.41	1.64 ± 2.43	0.26	5.27 ± 0.66	0.29	0.9994	3.84
CNT(T)-15-NR	0.92 ± 0.12	0.37	1.86 ± 0.67	0.29	5.10 ± 0.56	0.26	0.9978	3.66
CNT(T)-7-NP_300 °C	1.04 ± 0.14	0.41	2.24 ± 1.13	0.30	5.94 ± 1.28	0.26	0.9992	4.20

λ_{ex} : 370 nm, λ_{em} : 470 nm, filter: 435 nm; solid state, pure sample.

Table S2. EIS fitting parameters and determined components.

Sample	Condition	R1 (Ω)	C1 (F)	Q2 (F.s ^(a-1))	a2	R2 (Ω)	C2 (F)
CN(M)	Dark	8.511	11.93e-9	0.181e-3	0.734	22.3	32.23e-6
	Light	8.382	12.63e-9	0.133e-3	0.774	22.4	39.21e-6
CN(T)	Dark	7.817	3.86e-9	5.180e-3	0.017	18.0	2.26e-6
	Light	6.534	11.67e-9	2.870e-3	0.384	20.7	46.81e-6
CN(T)-15-NR	Dark	5.425	3.18e-9	0.189e-3	0.402	116.2	4.07e-6
	Light	4.323	4.27e-9	0.115e-3	0.589	90.46	18.5e-6
CN(T)-65-NR	Dark	2.012	5.24e-9	0.522e-3	0.999	209.0	28.77e-6
	Light	0.999	3.38e-9	63.89e-6	0.482	121.2	44.34e-6
CN(T)-14-NP	Dark	1.462	4.01e-9	0.492e-3	0.227	45.0	2.94e-6
	Light	0.821	3.13e-9	0.612e-3	0.356	131.0	4.53e-6
CN(T)-7-NP	Dark	0.360	3.54e-9	0.123e-3	0.379	109.4	3.38e-6
	Light	0.236	3.39e-9	22.06e-6	0.639	140.3	12.3e-6

Table S3. Comparison of pure water photo-splitting using different catalytic systems

Sl. No.	Catalyst	Light source	H ₂ yield ($\mu\text{mol g}^{-1} \text{h}^{-1}$)	Remarks
1.	SWCNT/2D C ₃ N ₄ heterojunction	300 W Xe lamp	49.8	26
2.	Red phosphorous/carbon nitride van der Waals heterostructure (RP-CN)	300 W Xe lamp	367.0	27
3.	3 wt%Pt–3 wt%CoP/g-C ₃ N ₄	300W Xe lamp	26.25	28
4.	Rh-RhO _x /PCN (polymeric carbon nitride)	300 W Xe lamp	28	29
5.	Boron phosphide@carbon nitride (BP@C ₃ N ₄)	300 W Xe lamp	31.5	30
6.	g-C _{3.6} N ₄	300 W Xe lamp > 420 nm	75.0	31
7.	Three-dimensional porous g-C ₃ N ₄ nanosheets (3D U-C ₃ N ₄ NS)	300 W Xe lamp	101.4	32
8.	Co(OH) ₂ /C ₃ N ₄ -Cl ₄ /Pt	300 W Xe lamp > 300 nm	48.2	33
9.	Ni single atom - PCN (polymeric carbon nitride)	300 W Xe lamp > 420 nm	26.65	34
10.	Pt-Co/g-C ₃ N ₄	300 W Xe lamp > 300 nm	12.2	35
11.	LaOCl/PCN (polymeric carbon nitride)	300 W Xe lamp > 300 nm	22.3	36
12.	Co-mCN	White LED (420 nm < λ < 700 nm)	1.82	37
13.	CN(T)-7-NP	300 W Xe, AM1.5G solar simulator	76.8	This work

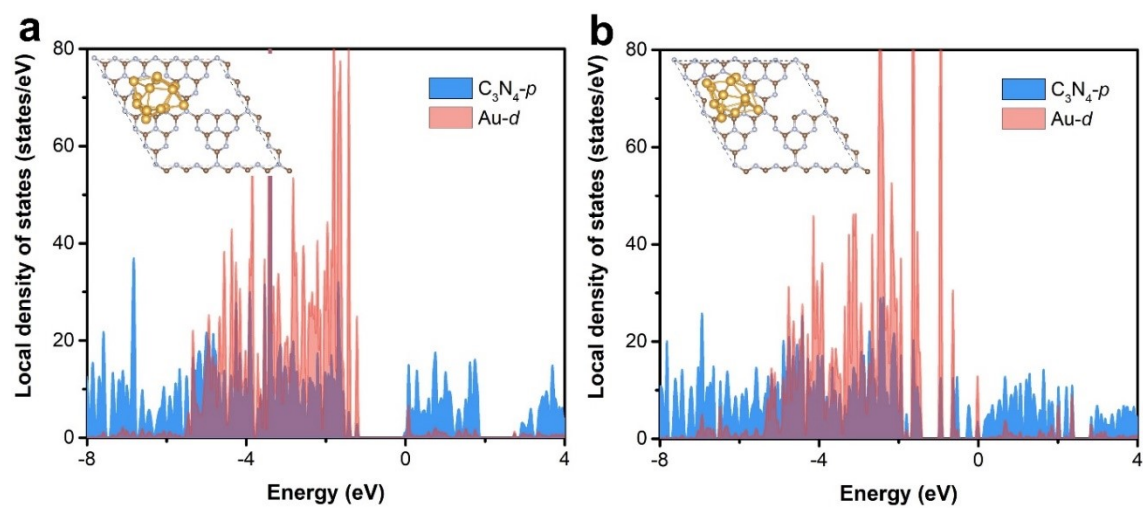


Figure S9. Local density of states of Au₁₃@CN without and with defects (**a** and **b**), where blue and red lines indicate the local density of states of CN-p orbits and Au-d orbits, respectively. Their corresponding geometric structures are shown in the insert. Yellow, silver, and grey balls indicate Au, N, and C atoms, respectively.

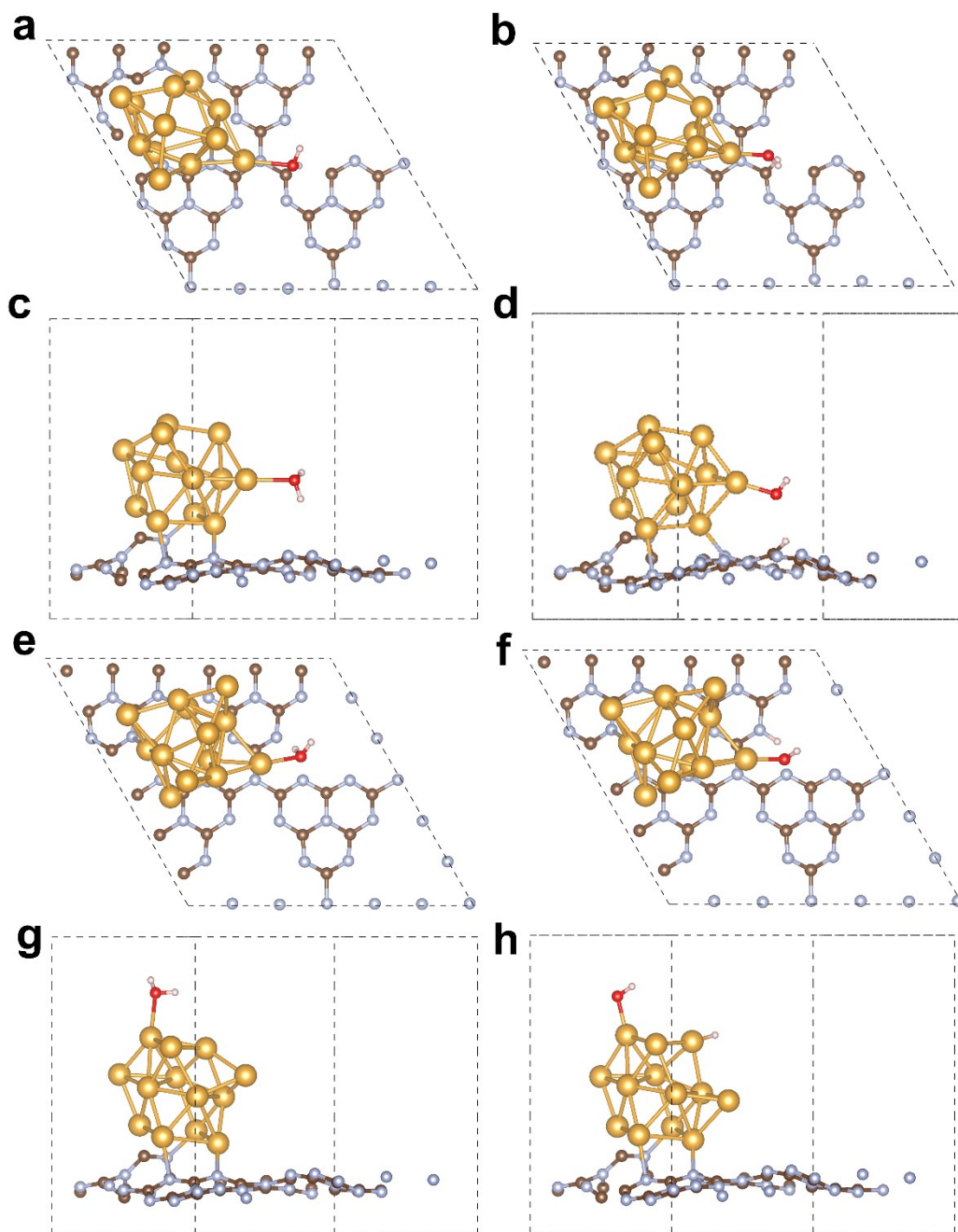


Figure S10. Geometric adsorption structures of H_2O^* and $\text{HO}^*\text{-H}^*$ on the interface with defects (**a-b**: top views; **c-d**: side views), interface without defects (**e-f**), and Au_{13} cluster (**g-h**). Yellow, grey, silver, red, and white balls indicate Au, C, N, O, and H atoms, respectively.

References

- 1 I. F. Silva, I. F. Teixeira, R. D. F. Rios, G. M. do Nascimento, I. Binatti, H. F. V. Victória, K. Krambrock, L. A. Cury, A. P. C. Teixeira and H. O. Stumpf, *Journal of Hazardous Materials*, 2021, **401**, 123713.
- 2 C. A. Simpson, K. J. Salleng, D. E. Cliffel and D. L. Feldheim, *Nanomedicine: Nanotechnology, Biology, and Medicine*, 2013, **9**, 257–263.
- 3 J. Turkevich, P. C. Stevenson and J. Hillier, *Discussions of the Faraday Society*, 1951, **11**, 55–75.
- 4 B. Nikoobakht and M. A. El-Sayed, *Chem. Mater.*, 2003, **15**, 1957–1962.
- 5 U. K. Thakur, A. M. Askar, R. Kisslinger, B. D. Wiltshire, P. Kar and K. Shankar, *Nanotechnology*, 2017, **28**, 274001.
- 6 A. F. G. Leontowich, A. Gomez, B. D. Moreno, D. Muir, D. Spasyuk, G. King, J. W. Reid, C. Y. Kim and S. Kycia, *Journal of Synchrotron Radiation*, 2021, **28**, 961–969.
- 7 G. Kresse and J. Furthmuller, *Phys. Rev. B: Condens. Matter Mater. Phys.*, 1996, **54**, 11169–11186.
- 8 P. E. Blöchl, *Phys. Rev. B: Condens. Matter Mater. Phys.*, 1994, **50**, 17953–17979.
- 9 J. P. Perdew, K. Burke and M. Ernzerhof, *Physical Review Letters*, 1996, **77**, 3865–3868.
- 10 S. Grimme, J. Antony, S. Ehrlich and H. Krieg, *Journal of Chemical Physics*, 2010, **132**, 154104.
- 11 W. Tang, E. Sanville and G. Henkelman, *Journal of Physics Condensed Matter*, 2009, **21**, 084204.
- 12 X. Hu, Z. Zhan, J. Zhang, I. Hussain and B. Tan, *Nature Communications*, 2021, **12**, 1–9.
- 13 L. Yang, J. R. Tumbleston, H. Zhou, H. Ade and W. You, *Energy and Environmental Science*, 2013, **6**, 316–326.
- 14 Y. Zhang, Z. Xu, Q. Wang, W. Hao, X. Zhai, X. Fei, X. Huang and Y. Bi, *Applied Catalysis B: Environmental*, 2021, **299**, 120679.
- 15 X. Wang, K. Klingan, I. Martens, A. Bagger, M. Klingenhof, T. Möller, J. F. De Araújo, S. Jiang, J. Rossmeisl, H. Dau and P. Strasser, *Nature Communications*, 2021, **12**, 1–12.
- 16 J. W. Wang, M. Gil-Sepulcre, H. H. Huang, E. Solano, Y. F. Mu, A. Llobet and G. Ouyang, *Cell Reports Physical Science*, 2021, **2**, 100681.
- 17 C. F. Holder and R. E. Schaak, *ACS Nano*, 2019, **13**, 7359–7365.
- 18 H. Borchert, E. V. Shevchenko, A. Robert, I. Mekis, A. Kornowski, G. Grübel and H. Weller, *Langmuir*, 2005, **21**, 1931–1936.
- 19 A. Monshi, M. R. Foroughi and M. R. Monshi, *World Journal of Nano Science and Engineering*, 2012, **2**, 154–160.
- 20 N. Meng, W. Zhou, Y. Yu, Y. Liu and B. Zhang, *ACS Catalysis*, 2019, **9**, 10983–10989.
- 21 Y. Xu, C. Qiu, X. Fan, Y. Xiao, G. Zhang, K. Yu, H. Ju, X. Ling, Y. Zhu and C. Su, *Applied Catalysis B: Environmental*, 2020, **268**, 118457.
- 22 J. Zhang, Y. Li, X. Zhao, L. Wang, H. Chen, S. Wang, X. Xu, L. Shi, L. C. Zhang, Y. Zhu, H. Zhang, Y. Liu, G. Nealon, S. Zhang, M. Wu, S. Wang and H. Sun, *Nano Energy*, 2021, **89**, 106357.
- 23 Y. Zheng, Y. Jiao, Y. Zhu, L. H. Li, Y. Han, Y. Chen, A. Du, M. Jaroniec and S. Z. Qiao, *Nature Communications*, 2014, **5**, 3783.
- 24 Y. Zhang, Q. Pan, G. Chai, M. Liang, G. Dong, Q. Zhang and J. Qiu, *Scientific Reports*, 2013, **3**, 1–8.
- 25 L. C. Chen, C. Y. Teng, C. Y. Lin, H. Y. Chang, S. J. Chen and H. Teng, *Advanced Energy Materials*, 2016, **6**, 1600719.
- 26 S. Wang, L. Chen, X. Zhao, J. Zhang, Z. Ao, W. Liu, H. Wu, L. Shi, Y. Yin, X. Xu, C. Zhao and X. Duan, *Applied Catalysis B: Environmental*, 2020, **278**, 119312.

- 27 M. Wang, Z. Qin, Z. Diao, R. Li, J. Zhong and Y. Chen, *ACS Sustainable Chemistry & Engineering*, 2020, **8**, 13459–13466.
- 28 Z. Pan, Y. Zheng, F. Guo, P. Niu and X. Wang, *ChemSusChem*, 2017, **10**, 87–90.
- 29 Z. Pan, S. Wang, P. Niu, M. Liu and X. Wang, *Journal of Catalysis*, 2019, **379**, 129–137.
- 30 B. Tian, Y. Wu and G. Lu, *Applied Catalysis B: Environmental*, 2021, **280**, 119410.
- 31 H. Liu, M. Shen, P. Zhou, Z. Guo, X. Liu, W. Yang, M. Gao, M. Chen, H. Guan, N. P. Padture, Y. Yu, S. Guo and S. Sun, *Nanoscale*, 2021, **13**, 9315–9321.
- 32 X. Chen, R. Shi, Q. Chen, Z. Zhang, W. Jiang, Y. Zhu and T. Zhang, *Nano Energy*, 2019, **59**, 644–650.
- 33 Q. Zhang, X. Chen, Z. Yang, T. Yu, L. Liu and J. Ye, *ACS Applied Materials and Interfaces*, 2022, **14**, 3970–3979.
- 34 Y. Li, Y. Wang, C. L. Dong, Y. C. Huang, J. Chen, Z. Zhang, F. Meng, Q. Zhang, Y. Huangfu, D. Zhao, L. Gu and S. Shen, *Chemical Science*, 2021, **12**, 3633–3643.
- 35 G. Zhang, Z. A. Lan, L. Lin, S. Lin and X. Wang, *Chemical Science*, 2016, **7**, 3062–3066.
- 36 Y. Lin, W. Su, X. Wang, X. Fu and X. Wang, *Angewandte Chemie - International Edition*, 2020, **59**, 20919–20923.
- 37 Y. Dou, C. Zhu, M. Zhu, Y. Fu, H. Wang, C. Shi, H. Huang, Y. Liu and Z. Kang, *Applied Surface Science*, 2020, **509**, 144706.